

# Supporting Information for

## Rosette Nanotube Porins as Ion Selective Transporters and Single-Molecule Sensors

Prabhat Tripathi,<sup>1</sup> Liang Shuai,<sup>2</sup> Himanshu Joshi,<sup>6</sup> Hirohito Yamazaki,<sup>1</sup> William H. Fowle,<sup>5</sup> Aleksei Aksimentiev,<sup>6,7\*</sup> Hicham Fenniri,<sup>2,3,4\*</sup> and Meni Wanunu<sup>1,3,4\*</sup>

<sup>1</sup>Department of Physics, Northeastern University, Boston, MA, 02115

<sup>2</sup>Department of Chemical Engineering, Northeastern University, Boston, MA, 02115

<sup>3</sup>Department of Chemistry & Chemical biology, Northeastern University, Boston, MA, 02115

<sup>4</sup>Department of Bioengineering, Northeastern University, Boston, MA, 02115

<sup>5</sup>Electron Microscopy Facility, Northeastern University, Boston, MA, 02115

<sup>6</sup>Department of Physics, University of Illinois at Urbana–Champaign, Urbana, Illinois 61801, United States

<sup>7</sup>Beckman Institute for Advanced Science and Technology, University of Illinois at Urbana–Champaign, Urbana, Illinois 61801, United States

E-mail: [aksiment@illinois.edu](mailto:aksiment@illinois.edu); [h.fenniri@northeastern.edu](mailto:h.fenniri@northeastern.edu); [wanunu@neu.edu](mailto:wanunu@neu.edu)

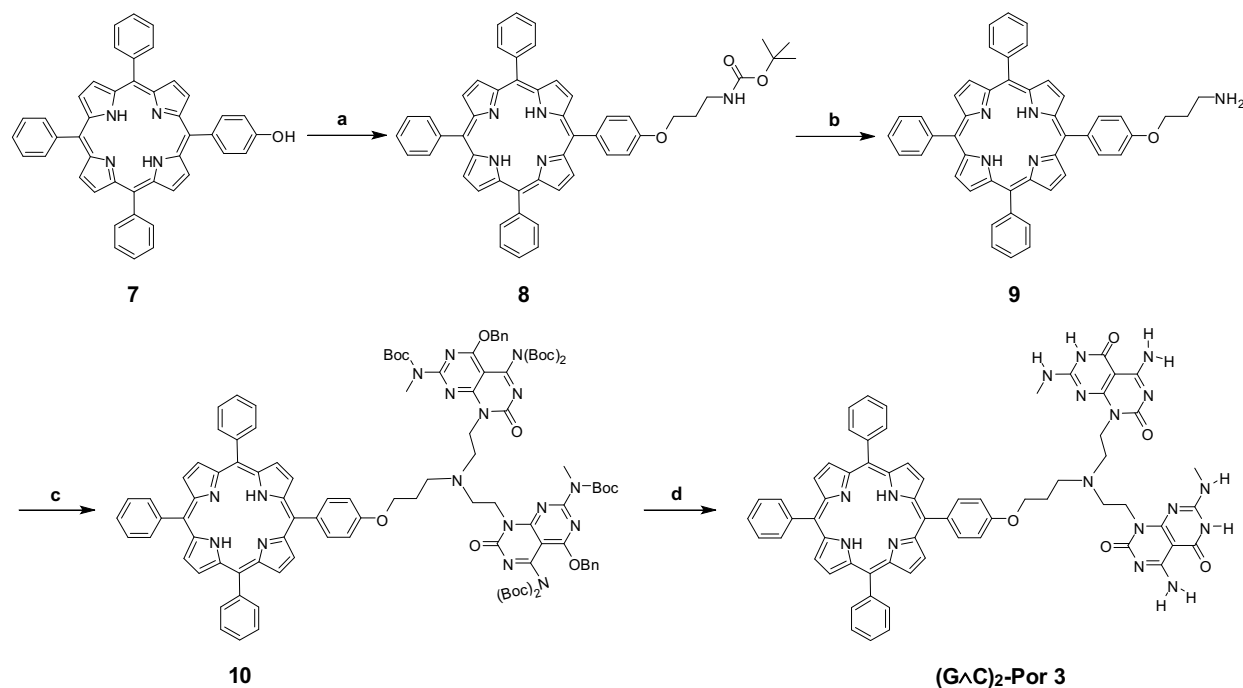
## Table of Contents:

- S1. Materials and Methods (3-9)
  - (A) Preparation of rosette nanotube porins (RNTPs) (3-7)
  - (B) Purification of RNTs (8)
  - (C) Reconstitution of RNTPs in lipid vesicles (8)
  - (D) Single-channel electrical recordings (8)
  - (E) Transmission electron microscopy measurements (9)
- S2. TEM images of RNTPs (10-11)
- S3. TEM images of RNTPs reconstituted in lipid vesicles (12)
- S4. Additional step-wise RNTP insertion events (13)
- S5. COMSOL simulation for RNTP conductance vs. length (14-15)
- S6. Noise spectrum of RNTP (16)
- S7. Ion-current traces for gating RNTPs (17-18)
- S8. Observations of step-wise decreases in ionic current (19-20)
- S9. Reversal potential measurements (21)
- S10. All-atom MD simulation of an RNTP embedded in lipid bilayer membrane (22)
- S11. Inter-event time distribution and  $\alpha$ -CD interaction with an RNTP (23-24)
- S12. Lifetime statistics of  $\alpha$ -CD interactions with an RNTP at different voltages (25)
- S13. All-atom MD simulation snapshots of  $\alpha$ -CD docked onto an RNTP (26)
- S14. Residual ionic current of  $\alpha$ -CD-bound RNTP from MD simulations (27)
- S15. All-atom MD simulation methodology (27-28)
- S16. SI References (29-30)

## S1. (A) Preparation of rosette nanotube porins (RNTPs).

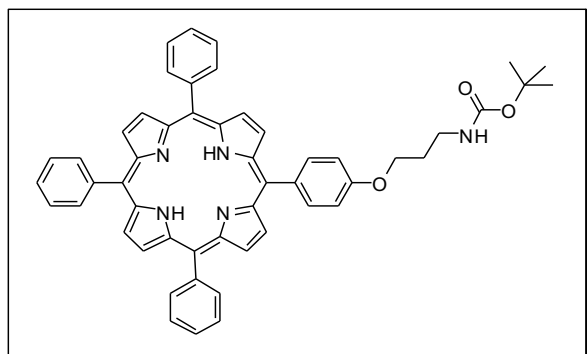
All of the commercially available reagents were purchased from Sigma-Aldrich or Acros Organics unless otherwise noted. NMR solvents were obtained from Cambridge Isotope Laboratories. Reagent grade solvents were purified using MBraun (SP05-172) solvent purification system, and all other commercial reagents were used as received. All of the reactions were performed under N<sub>2</sub> atmosphere using oven-dried glassware equipped with a magnetic stirring bar and rubber septum unless otherwise noted. Reactions were monitored by thin layer chromatography (TLC) using either silica or alumina-coated TLC plates (Macherey-Nagel) and visualized under UV light (Entela, UVGL-58). LC-MS (Agilent 1100 series) was also used when it was necessary. Silica (Silicycle, SiliaFlash F60, 230-400 mesh) and alumina (basic, Sigma-Aldrich, Brockmann I or II) were used for flash column chromatography. <sup>1</sup>H, <sup>13</sup>C and 2D NMR spectra were recorded on a 600 MHz Varian VNMRS 600 spectrometer at 298 K in the specific deuterated solvents noted in the synthetic procedures section. The NMR data is presented as follows: chemical shift, multiplicity (s = singlet, d = doublet, t = triplet, m = multiplet, br s = broad singlet, br t = broad triplet), integration, coupling constant, peak assignment. <sup>1</sup>H and <sup>13</sup>C NMR spectra were referenced relative to SiMe<sub>4</sub> using the chemical shifts of the NMR solvent residual peaks.

### Synthetic scheme of (GΛC)<sub>2</sub>-Por 3



Reagents and conditions: (a) 3-(Boc-amino)propyl bromide, Cs<sub>2</sub>CO<sub>3</sub>, KI, DMF, 65°C, 24 h; (b) DCM/TFA 1:1, 25°C, 2 h, followed by work-up with NaHCO<sub>3</sub>; (c) compound **1** (Figure 1(A) of main text), NaBH(OAc)<sub>3</sub>, triethylamine, THF, 4 d; (d) HCl (4 N, dioxane), 80°C, 4 h.

### 5-[4-(3-(Boc-amino)propoxy)phenyl]-10,15,20-triphenylporphyrin (**8**)



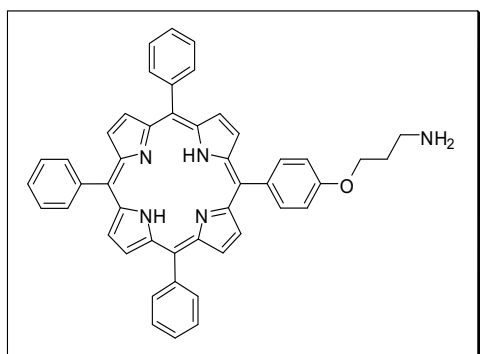
5-(4-Hydroxyphenyl)-10,15,20-triphenylporphyrin (compound **7**, 250 mg, 0.40 mmol, Frontier Scientific), 3-(Boc-amino)propyl bromide (124 mg, 0.52 mmol), Cs<sub>2</sub>CO<sub>3</sub> (195 mg, 0.60 mmol), KI (20 mg, 0.12 mmol) and DMF (10 mL) were added into a round bottom flask. The reaction mixture was stirred at 65°C for 24 h. The solvent was then removed under reduced pressure and the residue was dispersed in DCM (50 mL) and then filtered. The DCM in the filtrate was removed under reduced pressure, and the crude product was purified by flash column chromatography (alumina basic, n-hexane, 30% EtOAc) to provide **8** as a purple solid (305 mg, 0.39 mmol, 97%).

**<sup>1</sup>H NMR (600 MHz, CDCl<sub>3</sub>)**  $\delta$  (ppm): 8.88 (d, 2H, *J* = 4.2 Hz,  $\beta$ -pyrrole), 8.84 (s, 6H,  $\beta$ -pyrrole), 8.22-8.23 (m, 6H, ortho triphenyl), 8.13 (dd, 2H, *J* = 6.0 Hz, 1.8 Hz, meta phenol ether), 7.74-7.80 (m, 9H, meta/para triphenyl), 7.28 (dd, 2H, *J* = 6.0 Hz, 1.8 Hz, ortho phenol ether), 4.92 (br s, 1H, Boc-NH), 4.32 (t, 2H, *J* = 6.0 Hz, O-CH<sub>2</sub>-), 3.51 (q, 2H, *J* = 6.0 Hz, 6.0 Hz, CH<sub>2</sub>), 2.18 (t, 2H, *J* = 6.0 Hz, N-CH<sub>2</sub>-), 1.51 (s, 9H, Boc), -2.76 (s, 2H, pyrrole NH).

**<sup>13</sup>C NMR (125 MHz, CDCl<sub>3</sub>)**  $\delta$  (ppm): 158.8, 156.3, 142.4, 142.38, 142.35, 135.8, 134.9, 134.7, 134.6, 127.8, 126.8, 120.2, 120.1, 112.9, 79.5, 29.9, 28.6, 28.5.

**Positive LRMS (ESI):** Expected mass for (M+H<sup>+</sup>)/z, 788.4; Observed, 788.5 [M+H<sup>+</sup>]/z.

### 5-[4-(3-aminopropoxy)phenyl]-10,15,20-triphenylporphyrin (**9**)



5-[4-(3-(Boc-amino)propoxy)phenyl]-10,15,20-triphenylporphyrin (305 mg, 0.39 mmol) was dissolved in DCM (10 mL) in a round bottom flask and then TFA (10 mL) was added. The reaction mixture was stirred at 25°C for 2 h. The reaction was quenched by adding

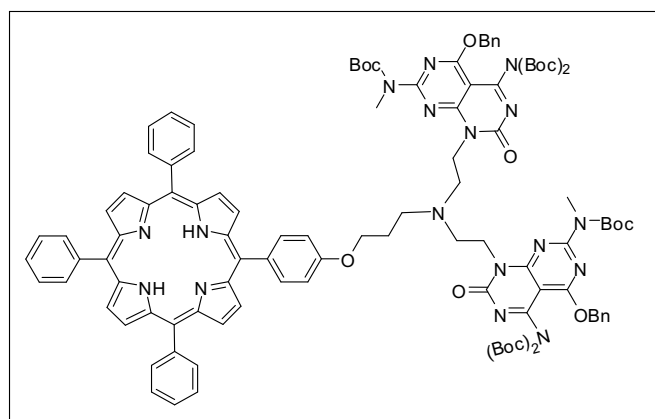
dd H<sub>2</sub>O (50 mL), followed by extraction with DCM (3 × 50 mL). The organic layer was neutralized by aqueous NaHCO<sub>3</sub> (5%, 2 × 50 mL), washed with dd H<sub>2</sub>O (50 mL), and brine (50 mL). The solvent was removed under reduced pressure to provide the pure product **9** as a purple solid (265 mg, 0.39 mmol, 100%).

**<sup>1</sup>H NMR (600 MHz, CDCl<sub>3</sub>)** δ (ppm): 8.89 (d, 2H, *J* = 4.8 Hz, β-pyrrole), 8.85 (s, 6H, β-pyrrole), 8.22 (d, 6H, *J* = 7.8 Hz, ortho triphenyl), 8.12 (dd, 2H, *J* = 6.0 Hz, 2.4 Hz, meta phenol ether), 7.74-7.80 (m, 9H, meta/para triphenyl), 7.28 (dd, 2H, *J* = 6.0 Hz, 1.8 Hz, ortho phenol ether), 4.35 (t, 1H, *J* = 6.0 Hz, O-CH<sub>2</sub>-), 3.10 (br s, 2H, N-CH<sub>2</sub>-), 2.13 (p, 2H, *J* = 6.6 Hz, CH<sub>2</sub>), 1.44 (br s, 2 H, NH<sub>2</sub>), -2.75 (s, 2H, pyrrole NH).

**<sup>13</sup>C NMR (125 MHz, CDCl<sub>3</sub>)** δ (ppm): 159.0, 142.4, 142.3, 135.8, 134.7, 131.2 (br), 127.8, 126.8, 120.25, 120.22, 120.1, 112.9, 66.3, 39.6, 33.5.

**Positive LRMS (ESI):** Expected mass for (M+H<sup>+</sup>)/z, 688.3; Observed, 688.5 [M+H<sup>+</sup>]/z].

### Compound **10**



To a round bottom flask, 5-[4-(3-aminopropoxy)phenyl]-10,15,20-triphenylporphyrin (200 mg, 0.29 mmol), compound **1** (280 mg, 0.44 mmol), triethylamine (0.08 mL, 0.58 mmol) and THF (15 mL) were added. The reaction mixture was stirred at 25°C under N<sub>2</sub> for 24 h before NaBH(OAc)<sub>3</sub> (123 mg, 0.58 mmol) was added. The reaction was quenched by adding aqueous NaHCO<sub>3</sub> (5%, 20 mL), and the mixture was extracted by DCM (3 × 50 mL). The organic layer was washed by dd H<sub>2</sub>O (50 mL), brine (50 mL) and dried over Na<sub>2</sub>SO<sub>4</sub>. The solvent was removed under reduced pressure and the residue was placed under high vacuum for 12 h. The procedure was repeated to move the reaction forward. Herein the residue was re-dissolved in THF (15 mL), and compound **1** (280 mg, 0.44 mmol) and triethyl amine (0.08 mL, 0.58 mmol) were added. After 24 h, NaBH(AcO)<sub>3</sub> (123 mg, 0.58 mmol) was added. The reaction mixture was stirred at 25°C under N<sub>2</sub> for 24 hours, followed by quenching and extraction in the same way above. The crude product was purified using flash column chromatography (Alumina basic, n-hexane, 30-50% EtOAc) to provide **10** as a purple solid (157 mg, 0.08 mmol, 28%).

**<sup>1</sup>H NMR (600 MHz, CDCl<sub>3</sub>)** δ (ppm): 8.89 (d, 2H, *J* = 4.8 Hz, β-pyrrole), 8.84 (s, 6H, β-pyrrole), 8.21-8.23 (m, 6H, ortho triphenyl), 8.10 (dd, 2H, *J* = 8.4 Hz, meta phenol ether), 7.73-7.79 (m, 9H, meta/para triphenyl), 7.45 (d, 4H, *J* = 6.6 Hz, ortho benzyl), 7.28-7.35 (m, 6H, meta/para benzyl), 7.27 (d, 2H, *J* = 7.8 Hz, ortho phenol ether), 5.59 (s, 4H, benzyl)



**Elemental Analysis:** Calculated for  $(C_{65}H_{56}N_{18}O_5) \cdot 7 (HCl) \cdot 6.1 (H_2O)$ , C: 51.31, H: 5.05, N: 15.65; Found: C: 51.30, H 5.02, N: 15.69.

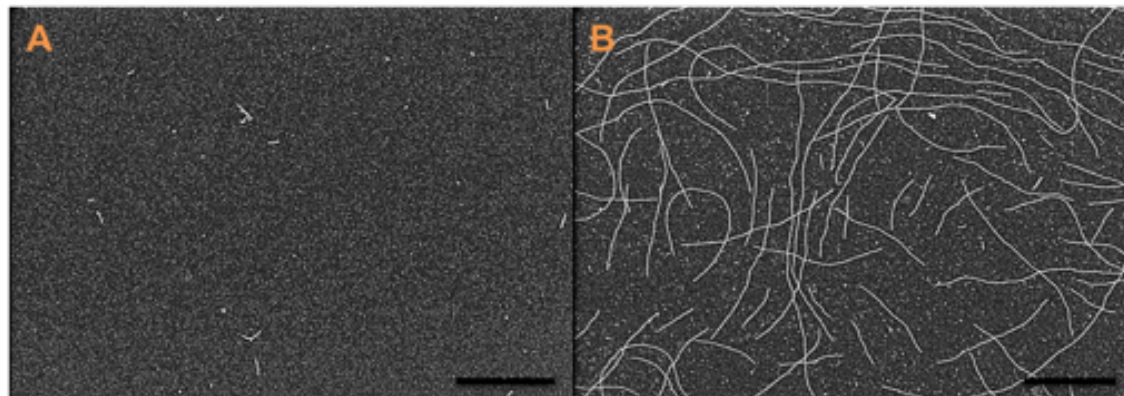


**Figure S1.** SEM images of a solution sample of  $(G^C)_2\text{-Por}$  before and after self-assembly. (A) 25 °C, aging for 1 min; (B) heating at 60°C for 3 min, aging for 10 min. Concentration: 0.07 mM in 1,2-DCB/MeOH (v/v, 9:1). Scale bar: 500 nm.

### **S1. (B) Purification of RNTs.**

Samples of RNTs were soluble in 1,2 dichlorobenzene (DCB) and contains hierarchy of RNTs with very wide distribution of its length as shown in SI: S2(A). To narrow down the length distribution of RNTP and to separate shorter tubes from longer, we diluted the RNTP samples (1mg/ml in 1,2 DCB), in methanol to a final concentration of 10 $\mu$ g/ml. Then we heated the resulting solution at 95°C for 20 minutes. The solution was then sonicated for 15minutes, and subjected to centrifuge for 15 minutes at 1300g (Fisher Scientific). Then 5-10  $\mu$ l of the centrifuged solution was added to lipid/chloroform solution to reconstitute purified RNTP in DPhPC lipid vesicle (as described in S1(C)).

### **S1. (C) Reconstitution of RNTPs in lipid vesicles.**

To incorporate RNTs into DPhPC liposomes, a 0.1 ml aliquot of 20 mg/ml of DPhPC in chloroform was added to a 5 ml glass vial and 5-10  $\mu$ l of purified RNTs (as described in S1(B)) was added to DPhPC/chloroform solution. The resultant solution was subjected to solvent rotatory evaporation for 20-30 minutes at 80-degree Celsius to leave a dried lipid and RNTP film. 1 ml of DI water or rehydration buffer (1M KCl, 10mM HEPES, 7.5 pH) was added to the vial and the mixture was hydrated followed by sonication for 1 minute. The solution was then extruded through a 200-nm-diameter pore polycarbonate membrane (Avanti polar lipid). TEM images validate the reconstitution of RNTP in lipid vesicles (S3).

### **S1. (D) Single-channel electrical recordings**

**Formation of perpendicular bilayer:** We used 1,2-diphytanoyl-*sn*-glycero-3-phosphocholine (DPhPC, purchased from Avanti Polar Lipid.) to form perpendicular phospholipid bilayer across an aperture (diameter, 50  $\mu$ m) in a Teflon film separating the two compartments (1 ml each *cis/trans*) of the polytetrafluoroethylene (PTFE) flow cell apparatus. We used standard method of Montel-Muller technique to form lipid bilayer on PTFE aperture<sup>1,2</sup>.

**Buffer solution:** 1M potassium chloride (KCl) solutions in 10 mM 2-[4-(2-hydroxyethyl) piperazin-1-yl] ethanesulfonic acid (HEPES) in deionized water (18 M $\Omega$ cm) were prepared for measurements. The pH of the buffer solution was adjusted to 7.5 by adding 1M potassium hydroxide (KOH).

**Electrical measurements and data analysis:** Ionic currents were measured by using Ag/AgCl electrodes with a patch-clamp amplifier (Axopatch 200B, Molecular Devices, Axon Instruments). The amplified signal was low-pass-filtered at 5 kHz (or 10 kHz) and acquired at 250 kHz using the Digi Data 1200 digitizer with a custom National Instruments LabVIEW program. The recorded ionic current traces were analyzed using, Python, and plotted in Igor Pro and in Origin Pro software.

**$\alpha$ -cyclodextrin:**  $\alpha$ -CD hydrate 98 +% was purchased from ACROS organics and incorporated in buffer solution to evaluate sensing using RNTPs.

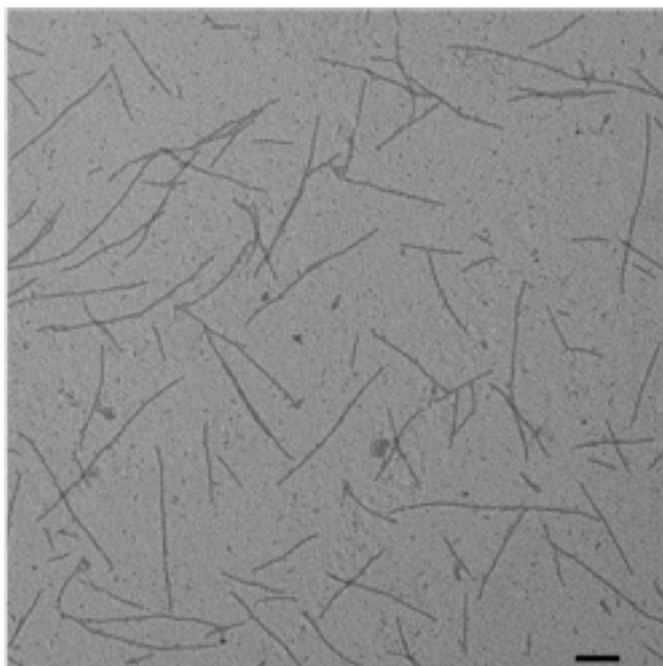
### **S1. (E)Transmission electron microscopy measurements.**

Particles were adsorbed on glow-discharged formvar-supported carbon-coated Cu300 TEM grids (Electron Microscopy Sciences). We used unstained sample for imaging of RNTP in 1,2 DCB. For imaging of RNTPs reconstituted in vesicles, grids for transmission electron microscopy were prepared by negative staining, using 2% uranyl acetate solution. Images were taken on a JEOL JEM TEM-1010 at 80 kV.

## S2. TEM images of RNTPs

### (A) Unpurified RNTPs

(i)



(ii)

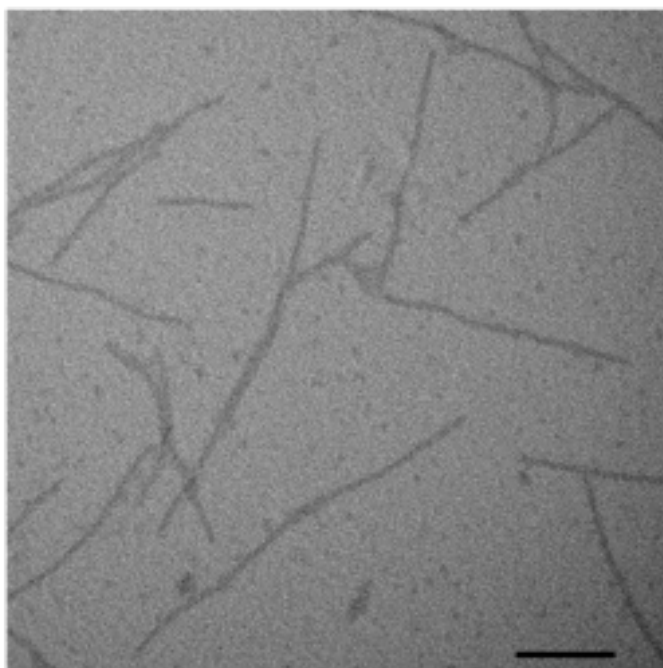


**Figure S2(A)** (i) Air dried TEM images of unpurified RNTPs at 20kx magnification and (ii) at 50kx magnification. Scale bars are 100nm.

### **(B) Purified RNTPs**

The unpurified RNTPs consist of very long RNTPs of length longer than 200 nm and are not suited for single-channel conductance experiments. Purification (See (S1(B))) filters long RNTPs and renders only shorter RNTPs.

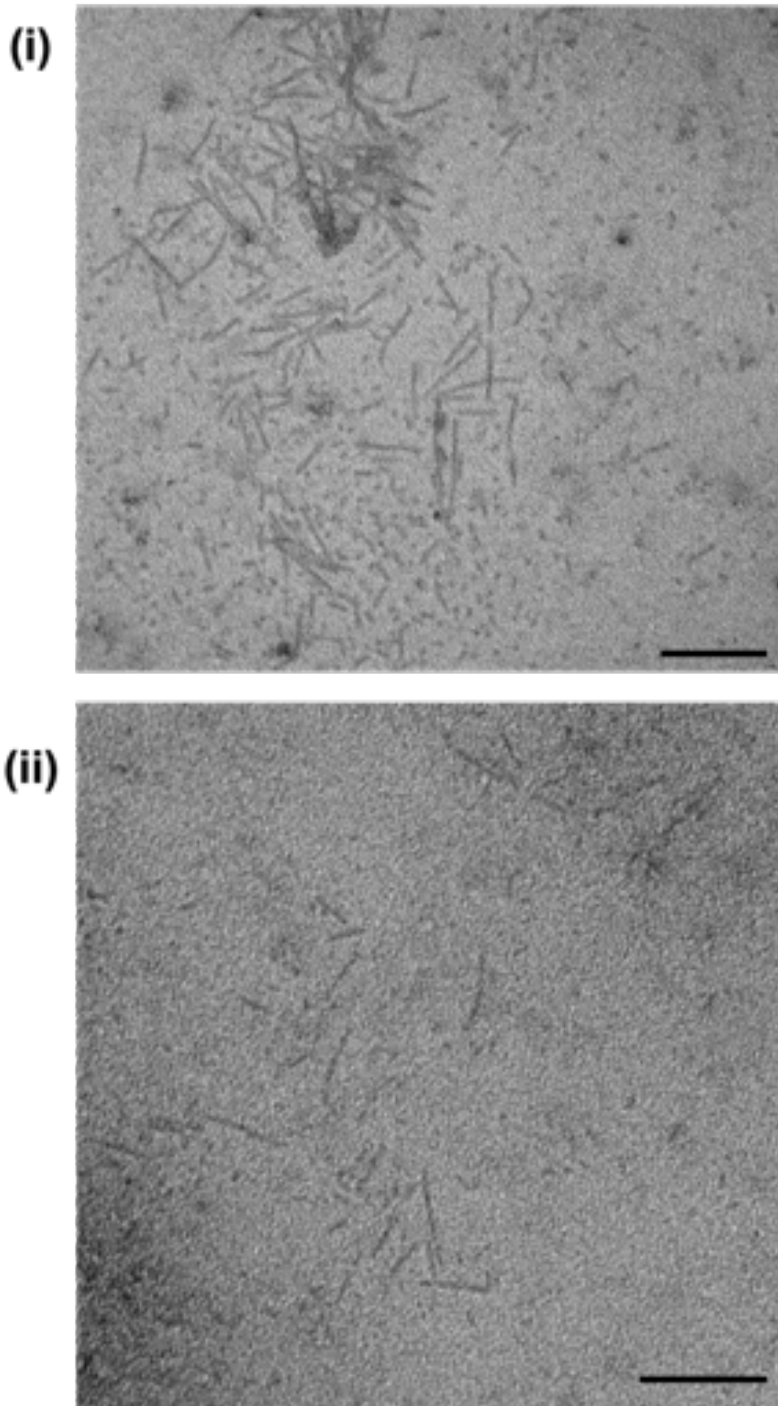


**Figure S2(B)** (i) Air dried TEM images of purified RNTPs at 50kx magnification and (ii) at 60kx magnification. Scale bars are 100nm.

**S3. TEM images of RNTPs reconstituted in lipid vesicles.**

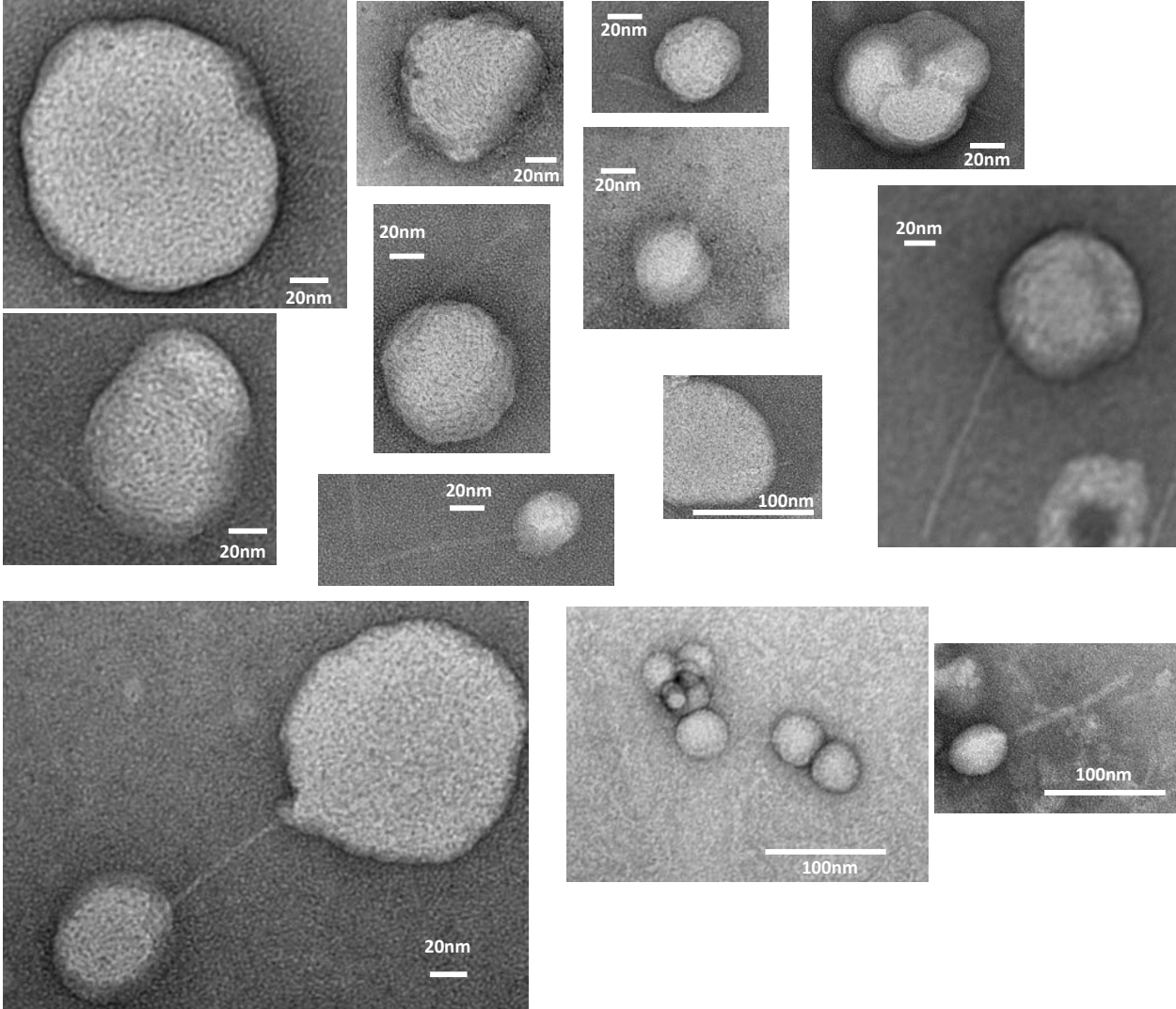
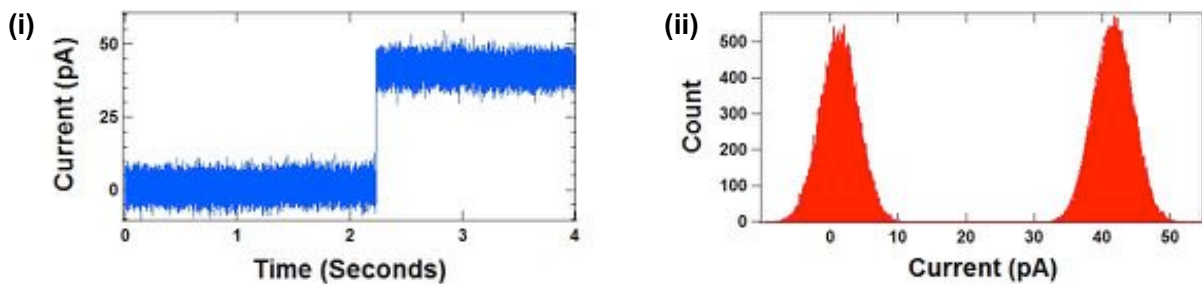


**Figure S3** Various TEM images of negative-stained RNTPs reconstituted in lipid vesicles.

#### S4. Additional stepwise RNTP insertion events.

(A)



(B)

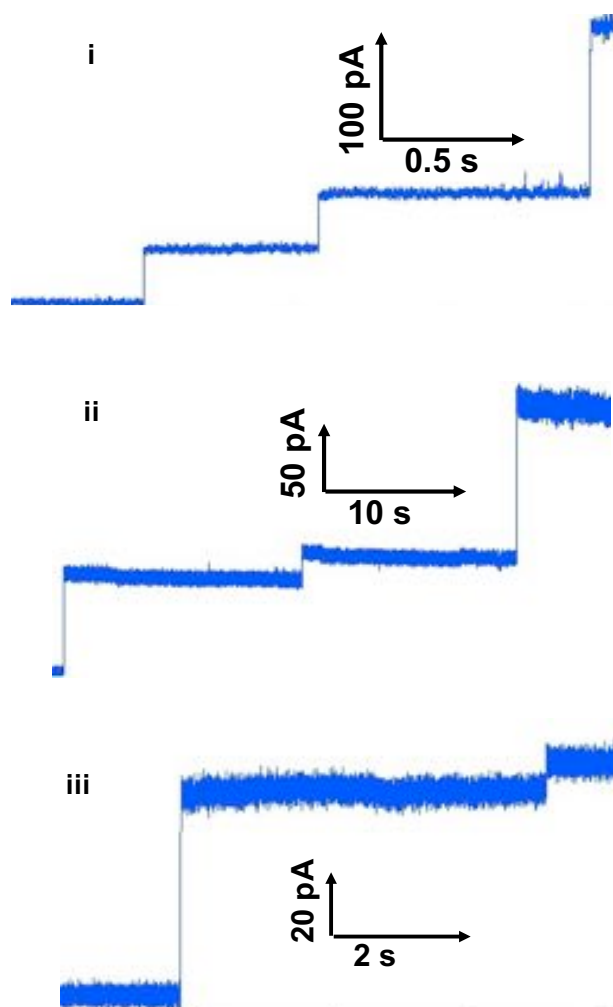


**Figure S4(A)** Ionic current trace showing (i) insertion of single RNTP of length 25nm and (ii) histogram current trace,  $n=161139$ . **(B)** Additional signature of stepwise insertions of RNTPs of different lengths into the lipid bilayer. All the data for 1M KCl, 10mM HEPES 7.5 pH, and at 100 mV and displayed after low-pass-filtering at 5kHz.

## S5. COMSOL simulation for RNTP conductance vs. length.

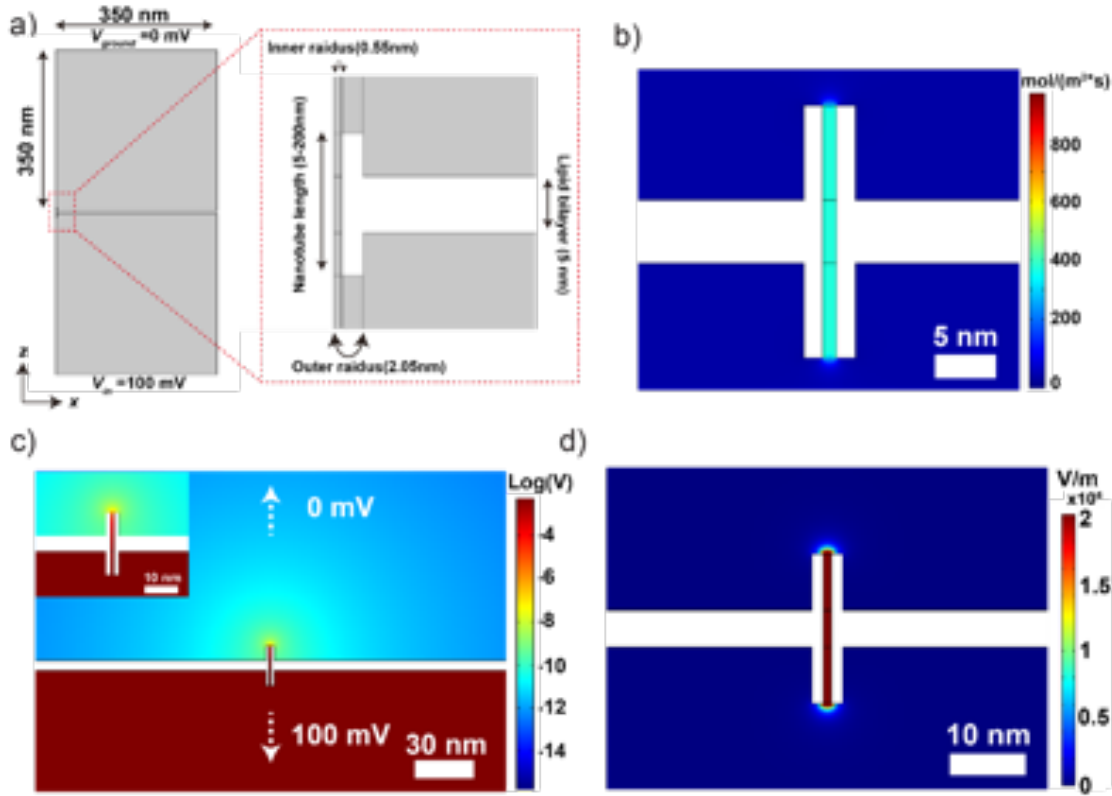


**Figure S5** (a) The geometry of our RNTP model. The applied voltage  $V_{in} = 100\text{mV}$  and the ground  $V_{ground} = 0\text{mV}$  were implemented on the bottom and top boundary, respectively. The model was designed to have 0.55 nm inner radius and 2.05 nm outer radius of RNTP embedded into the lipid bilayer with 5 nm thickness. (b), (c), (d) Profiles of the potassium ion flux along z axis, the electrical potential and the electric field around the 20 nm long RNTP at 100 mV.

The steady-state finite element simulation, COMSOL Multiphysics, was used to estimate the ion current through an RNTP as a function of its length. The Poisson-Nernst-Planck (PNP) Stokes system which describes the coupling between ion transport, electric field and hydrodynamics consists of the Navier-Stokes equation (1),

$$\rho(\mathbf{u} \cdot \nabla)\mathbf{u} = \nabla P + \eta \nabla^2 \mathbf{u} - F \left( \sum_i z_i c_i \right) \nabla \Phi \quad (1)$$

the Nernst-Planck equation (2)

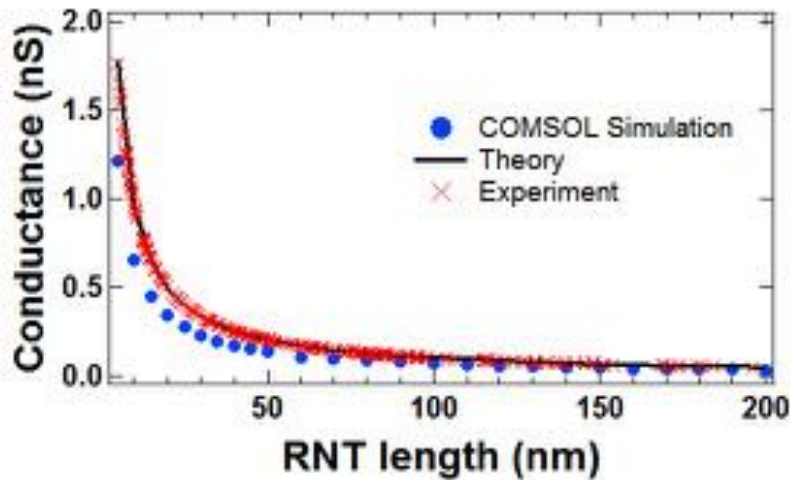
$$\mathbf{J}_i = -D_i \nabla c_i - \frac{F z_i}{RT} D_i c_i \nabla \Phi + c_i \mathbf{u} \quad (2)$$

and the Poisson's equation (3).

$$\nabla^2 \Phi = -\frac{F}{\epsilon} \sum_i z_i c_i \quad (3)$$

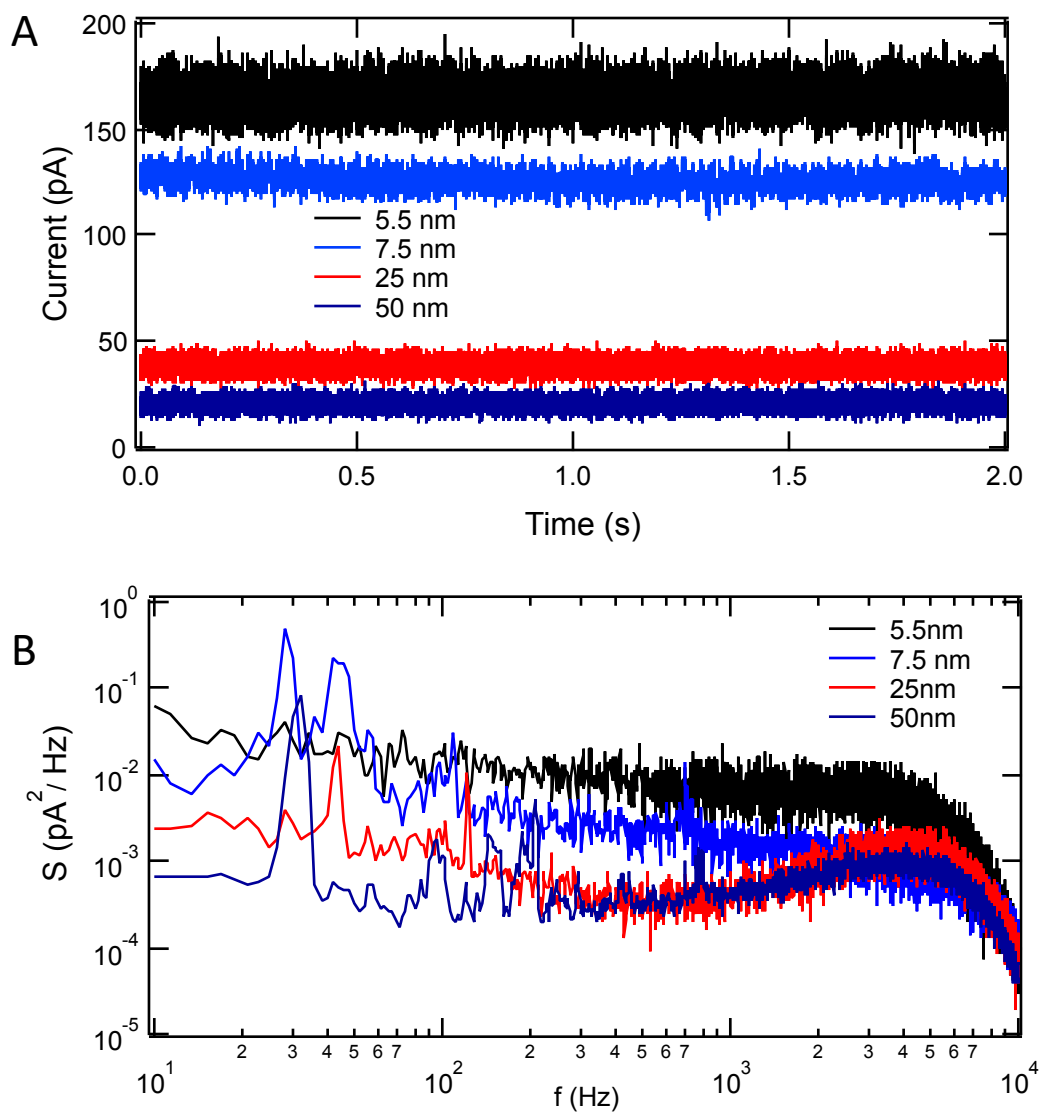
In the equations above,  $\mathbf{u}$ ,  $\Phi$ ,  $P$  and  $\mathbf{J}_i$  are the fluid velocity, the electrical potential, the pressure and the ion flux.  $z_i$ ,  $c_i$  and  $D_i$  are charge, concentration and the diffusion coefficient of species  $i$  in the solution.  $\rho$ ,  $\eta$ , and  $\epsilon$  are the density, the viscosity and the permittivity of the solution.  $F$ ,  $R$  and  $T$  are the Faraday's constant, the gas constant and the absolute temperature respectively. In the COMSOL, we used Transport of diluted species, Laminar flow and Electrostatics module for the calculation of osmosis velocity. The solution parameters were chosen to correspond to a KCl solution ( $D = 2 \times 10^{-9} \text{ m}^2/\text{s}$ ,  $c_{\text{K}^+} = c_{\text{Cl}^-} = 1 \text{ M}$ , and  $T = 298 \text{ K}$ )

Figure S5 (i) (a) shows the geometry of our model. The RNTP length ranges from 5 to 200 nm. The inner and outer radius of RNTP were 0.55 and 2.05 nm, respectively. Thickness of lipid bilayer was 5 nm. We employ the applied voltage  $V_{in} = 100 \text{ mV}$  on the bottom boundary and ground  $V_{ground} = 0 \text{ mV}$  on the other side. The exterior compartments of nanopore were extended 50 nm toward  $r$ - and  $z$ - axis from nanopore opening. No slip boundary condition was applied for the all boundary. Zero surface charge,  $0 \text{ C}/\text{m}^2$ , was chosen for all boundary. The ionic current through RNTP in Figure • was calculated by multiplying the integrated flux toward  $z$  axis in RNTP to Faraday constant ( $9.6 \times 10^4 \text{ s A/mol}$ ).



**Figure S5 ii** The Conductance of an RNTP with its length. Cross markers are experimentally observed conductance values from the RNTP and estimated lengths from theory (reference 24 in main text).

## S6. Noise spectrum of RNTP.



**Figure S6 (A)** Ionic current traces of single channel RNTPs of different lengths (indicated) measured at 100 mV, in 1M KCl, 10mM HEPES, 7.5 pH and low-pass filtered at 5kHz. **(B)** Noise spectra of the traces shown in **(A)**.

**S7. Ion-current traces for gating RNTPs.**

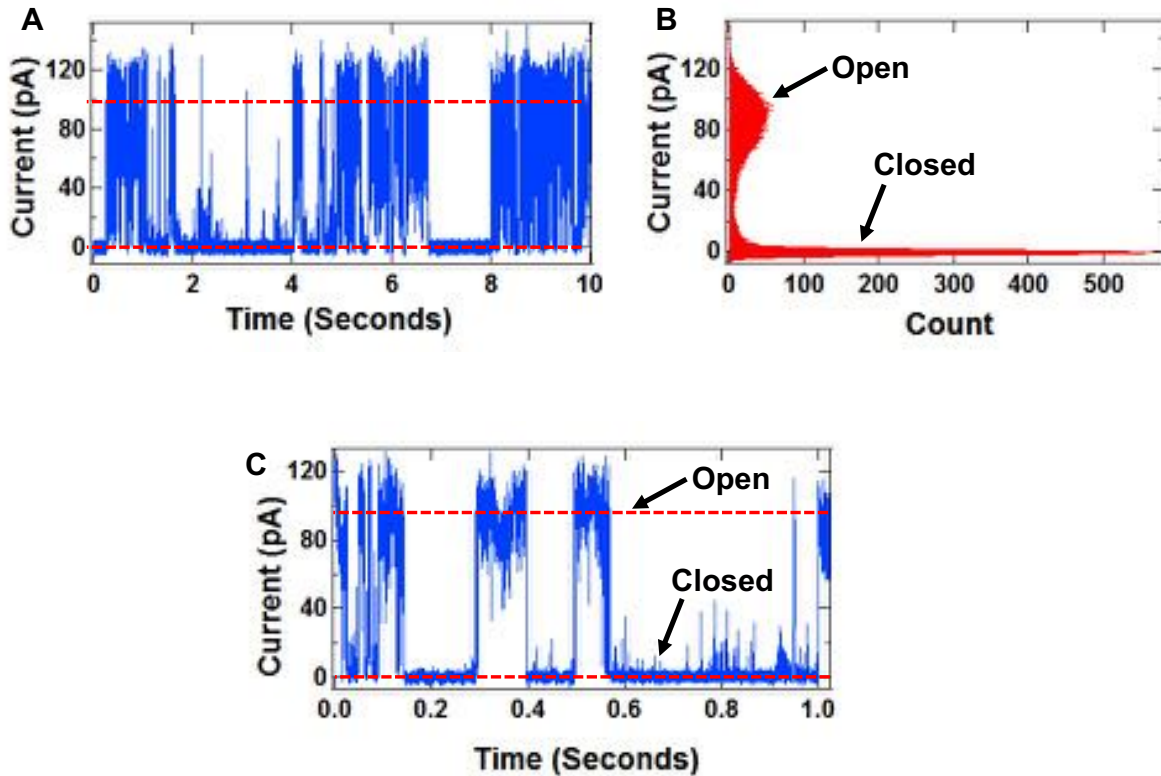


**Figure S7 (i)** (A) Ionic current trace showing gating behavior of RNTP undergoing closed and open states. (B) Histogram of current traces ( $n = 269,696$ ). All the data for 1M KCl, 10mM HEPES 7.5 pH, and at 100 mV and were recorded at 5 kHz. (C) Zoomed-in view of a current recording showing gating events (expanded from current trace shown in (A)).

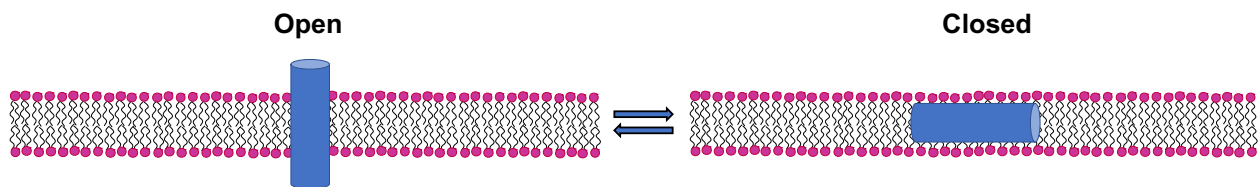


**Figure S7 (ii)** (A) A proposed model for observed gating in RNTPs. The RNTP can tilt completely in lipid bilayer to maximize its hydrophobic interaction. The observed opening and closing of an RNTP may be due to reversible tilting.

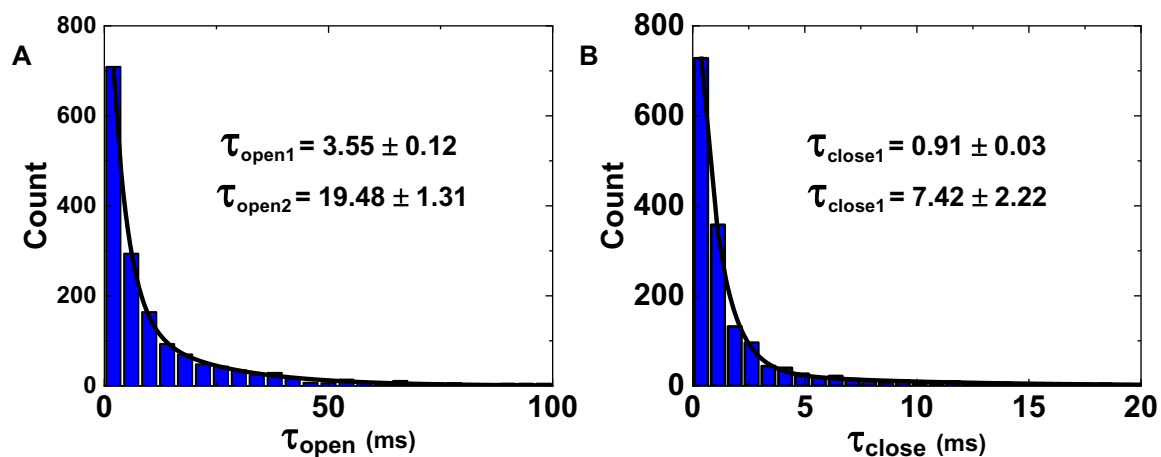


**Figure S7 (iii)** (A) Histogram of open state lifetimes, in ms ( $n = 1,713$ ) and double exponential fit of the histogram (black curve). The contribution of the slower timescale events is 47%. (B) Histogram of closed state lifetimes, in ms ( $n = 1,715$ ), and double exponential fit of the histogram (black curve). The contribution of the slower timescale events is 22%.

## S8. Observations of step-wise decreases in ionic current.

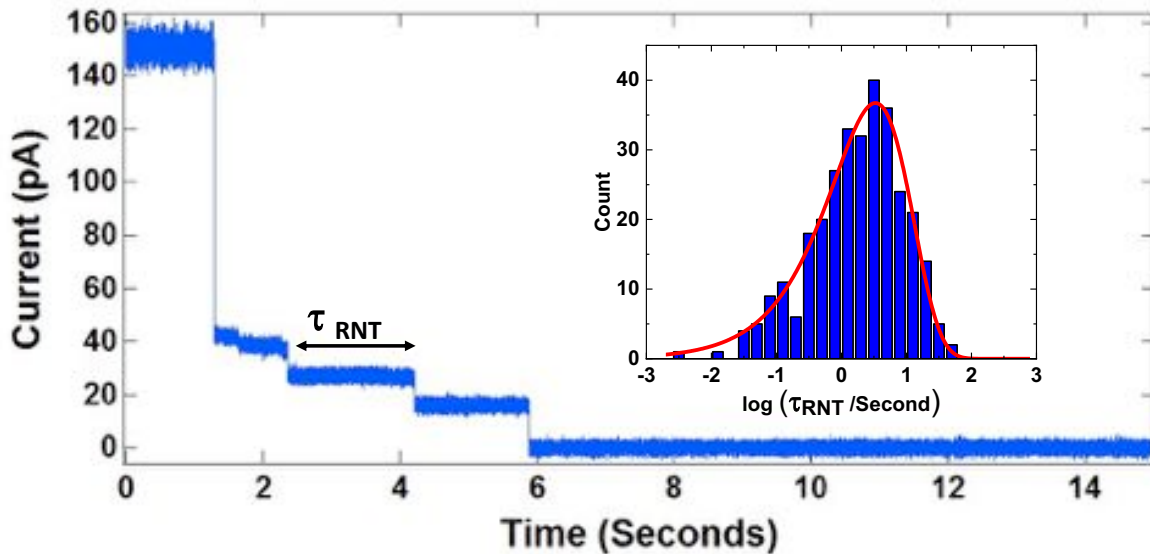


**Figure S8(i)** Ionic current trace showing step-wise decreases in ionic current. Inset figure shows a log-lifetime histogram for each discrete conductance level observed, along with a log Weibull distribution fit of the histogram (time constant of 3.33 seconds). All the data for 1M KCl, 10mM HEPES 7.5 pH, and at 100 mV.

We also observed a type of events, where ionic current due to insertion of several RNTPs decreases in a stepwise manner as shown in Figure S7. This type of events has been observed for DNA barrels in lipid bilayer and interpreted as separate pore closure<sup>3</sup>. However, the detail mechanism behind the pore closures is unknown. In our experiments, this may be due to three possibilities: (i) diffusion/translation-driven migration of RNTPs from lipid bilayer to hexadecane annulus (See Figure S7(ii)) or (ii) tilting of RNTP so that the hydrophobic exterior of the RNTP is exposed to the lipid environment, as shown in Figure S6 (ii), or (iii) there can be a possibility of translocation of RNTPs through the lipid bilayer as seen for ultrashort CNT<sup>4</sup>. Case iii is less likely as porphyrin modified RNTPs would like to be in lipid bilayer rather going into aqueous phase.



**Figure S8 (ii)** Schematic of artificial lipid bilayer setup showing the hexadecane region where RNTP can migrate.

To understand these possibilities, we first hypothesized that individual discrete decrease in conductance are due to elimination of RNTPs from lipid bilayer. and estimated the length of eliminated RNTP using analytical equation (ref 24 in main text). For example, in trace shown in Figure S7(i), the current first drops from  $150.40 \pm 0.02$  pA to  $41.13 \pm 0.09$  pA at 100mV, causing conductance drop of  $1.09 \pm 0.08$  nS, and elimination of  $\sim 8.7$ nm long RNTP. Similarly, the current almost vanishes, because of the elimination of RNTPs with length 74 nm, 126.23 nm, and 64 nm respectively. We estimated lengths of 271 such eliminations and constructed the histogram. We expected that, if these stepwise decrease in current are due to elimination of RNTPs, then distribution of lengths of eliminated RNTPs must resemble the distribution of length of RNTPs inserted in lipid bilayer (Figure 2(D) in main text). Indeed, we find that the histograms of estimated length of eliminated RNTPs (Figure S7 (iii)) resemble to the histogram of length of inserted RNTPs.

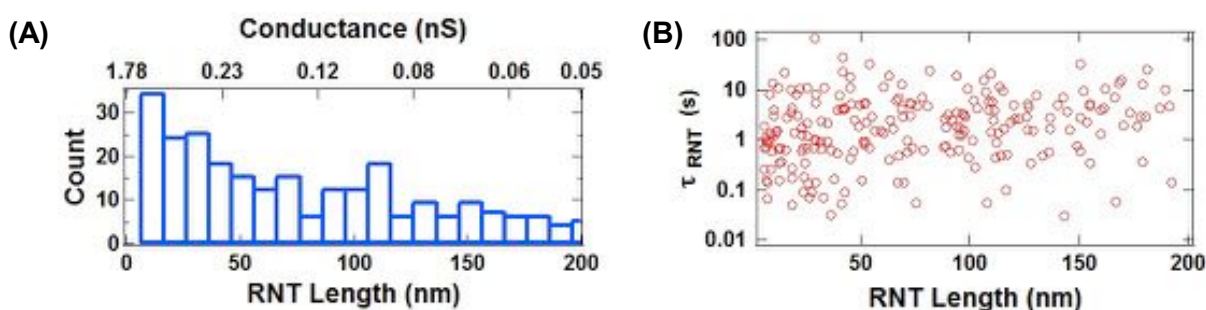


**Figure S8 (iii)** (A) Histogram of RNT length of RNTP closures. (B) Lifetime of each RNTP is plotted against its length. Both plots are from 271 events. All the data for 1M KCl, 10mM HEPES 7.5 pH, and at 100 mV.

We also explored the correlation between lifetimes for the elimination of RNTPs with its length. We find that the lifetimes for the elimination of RNTPs and its length are not correlated. This suggest that the migration of RNTPs into the hexadecane annulus are less likely. If RNTPs are migrating into hexadecane annulus *via* diffusion, then longer RNTPs are expected to diffuse slowly in lipid bilayer. Furthermore, if one assumes an RNTP diffuses isotopically in two-dimensional lipid bilayer, the diffusion coefficient of RNTP of length 15 nm which has been displaced  $\sim 100\mu\text{m}$  (approximated dimension of the lipid bilayer) in 3.33 s (Fig S7 (i)) will be  $\sim 750 \mu\text{m}^2/\text{s}$ . This diffusion is approximately 100-fold faster compare to the lateral diffusion of proteins in a lipid bilayer<sup>5</sup>. Therefore, case (ii) which is tilting of RNTPs in lipid bilayer is perhaps more likely to account for the stepwise decrease in current, and will require further computational and experimental investigations.

## S9. Reversal potential measurements.

For reversal potential measurements, we follow the strategy of recent report<sup>6</sup>. The chambers were filled with different salt solutions as noted in the main text. The I-V curves were corrected for the redox potential of the electrodes by the theoretical value for the redox potential, Theoretical redox potential values were calculated using the Nernst equation given below.

$$\Delta E = \frac{RT}{F} \ln \left[ \frac{a_{trans}}{a_{cis}} \right] \quad (4)$$

where  $\Delta E$  is the theoretical potential offset observed at the electrodes, R is the gas constant, T is the temperature of the solution, F is the Faraday constant, and a is the activity of the ionic species<sup>7</sup>. The reversal potential was then used with the Goldman-Hodgkins-Katz equation to extract the transference numbers for the membrane  $t_M$ .

$$(2 t_M - 1) = \frac{V_r}{\Delta E} \quad (5)$$

Here  $V_r$  is the corrected reversal potential. With the knowledge of effective transference number of membrane and cation transference number  $t_s$  in bulk solution (0.49 for KCl)<sup>8,9</sup>, the permselectivity P of the membrane

$$P = \frac{t_M - t_s}{1 - t_s} \quad (6)$$

and selectivity ratio (cation/anion) can be calculated as

$$SR = \frac{t_M}{1 - t_s} \quad (7)$$

## S10. All-atom MD simulation of RNTP embedded in lipid bilayer membrane.

To obtain a molecular account of water and ion permeation through RNTP, we created all-atom models of RNTP embedded in POPC lipid bilayer membrane with explicit water and ions (see the simulation methodology S14 for details). Figure S9A shows the cut-away side view of the simulated system. As the simulation proceeds, water and ions start permeating across the membrane through the RNTP as shown in figure S9b. There exist two separate permeation networks in the RNTP, one through the central lumen surrounded by G-C pairs and other is along the outer periphery near the porphyrin molecules as illustrated in figure S9C-E. We observed that the central lumen, figure S9C, only allows the permeation of cations ( $K^+$  or  $Na^+$ ) whereas the outer porous region only permeates anions ( $Cl^-$ ).

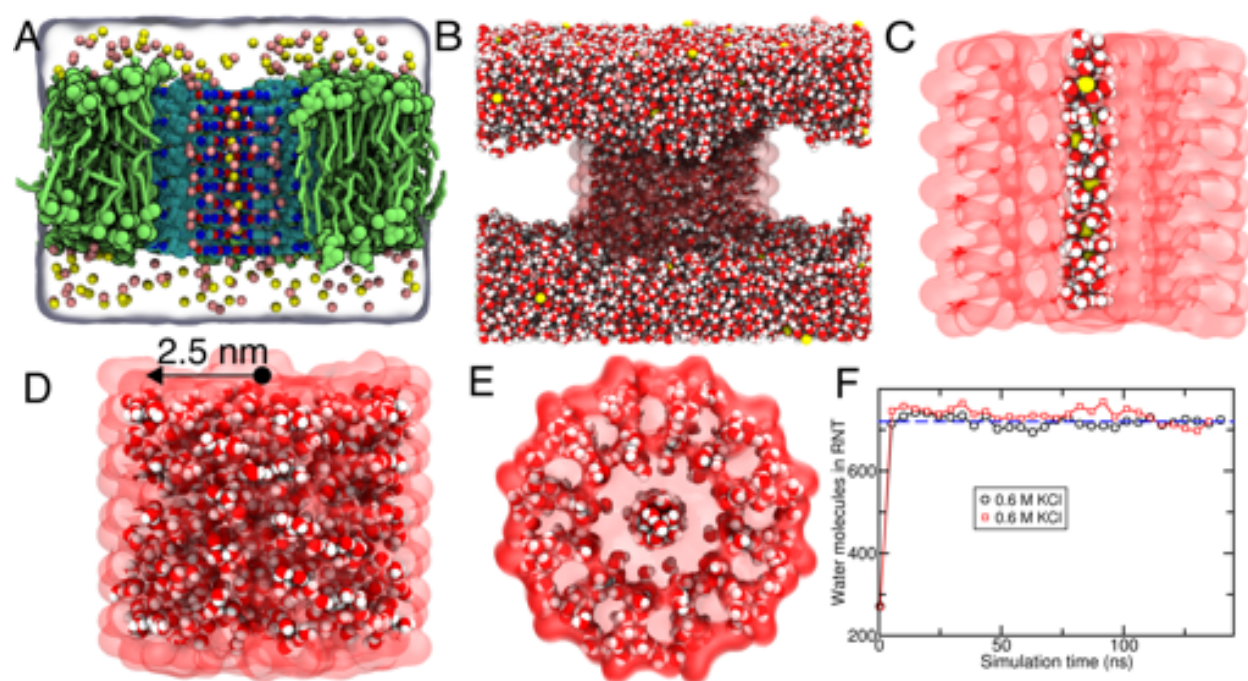


**Figure S10. MD simulation of RNTP in a lipid bilayer membrane.** (A) Cut-away side view of the simulated system at the end of a 150 ns equilibration simulation. Lipid molecules are shown in green whereas water is shown as a white semi-transparent surface, the representation scheme of RNTP and ions is similar to that from figure 2G. (B) All water molecules and ions in the simulated system. (C) A snapshot highlighting the water and ions present in the central lumen of RNTP (cut-away side view). On an average, six hydrated  $K^+$  (yellow sphere) are always present inside the central lumen of the channel. (D,E) Snapshots showing the (D) side view and (E) top view of the water molecule network within the RNTP. In panels B-E, water molecules are shown in red (oxygen) and white (hydrogen) spheres and RNTP is shown in transparent red background. (F) The total number of water molecules present in the transmembrane region as a function of simulation time as shown in figure D or E. On an average, there

are 750 water molecules (blue line) present in the RNTP channel in both of the simulated system, 0.6 M NaCl and 0.6 M KCl.

### S11. Inter-event time distribution and $\alpha$ -CD interaction with an RNTP

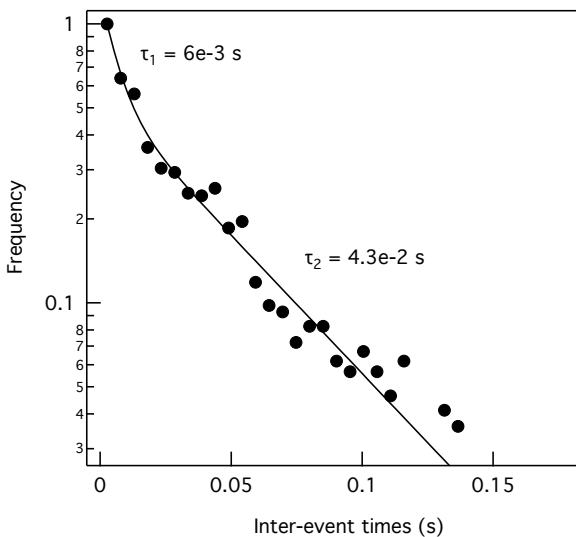


**Figure S11(i).** The distribution of inter-event times for 200  $\mu$ M  $\alpha$ -CD measured at 75mV. Solid black line is double exponential fit of the distribution with time constants 6.1 ms (48 % contribution) and 43.8 ms (52% contribution). The very fast timescale (minor population) is most likely unbinding/rebinding of the same molecule to the pore, whereas the slower timescale is related to arrival of a molecule from bulk to the pore.

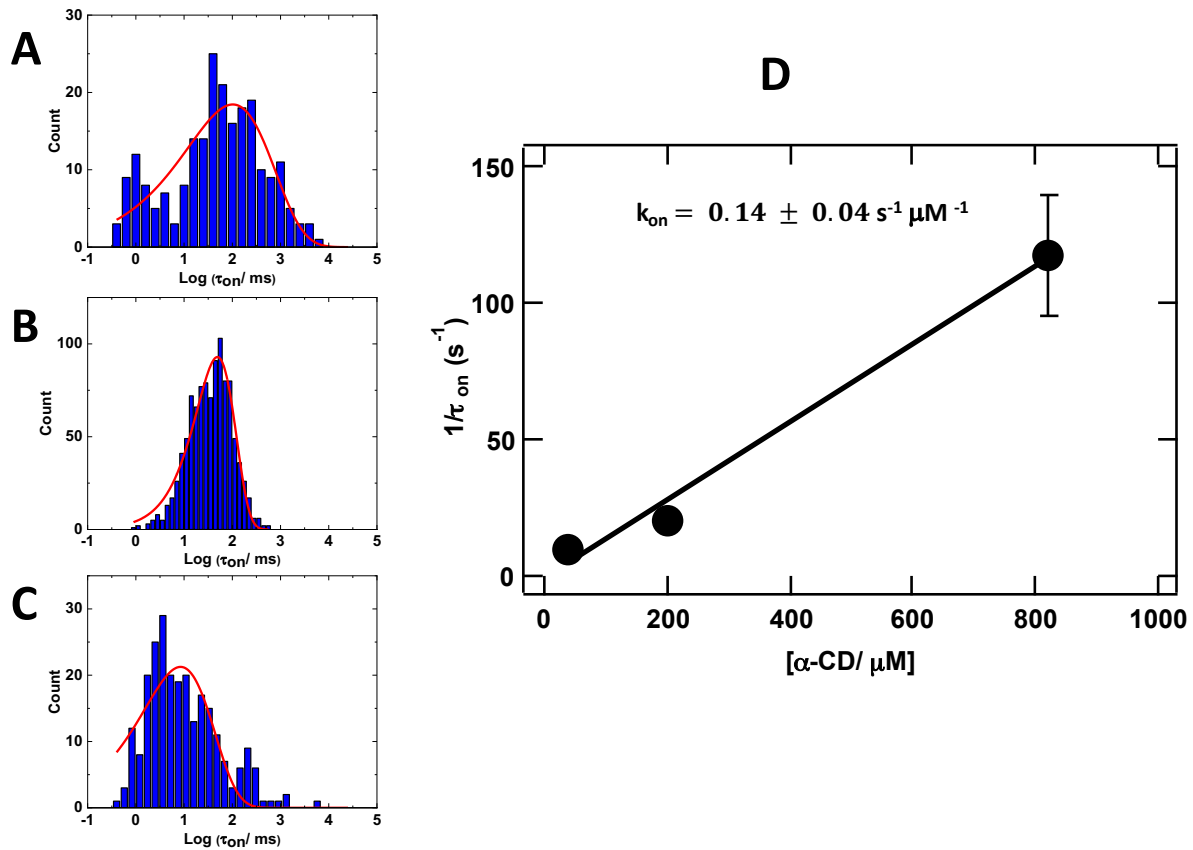
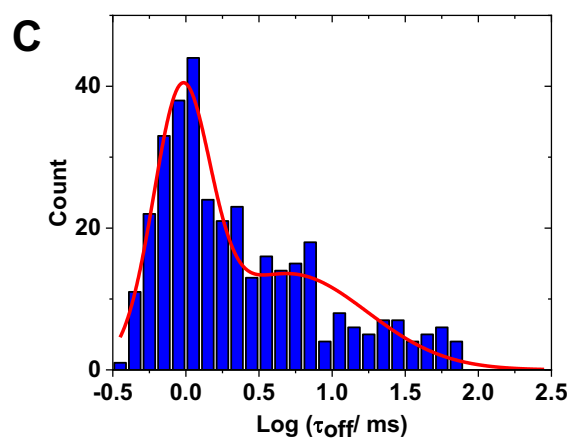
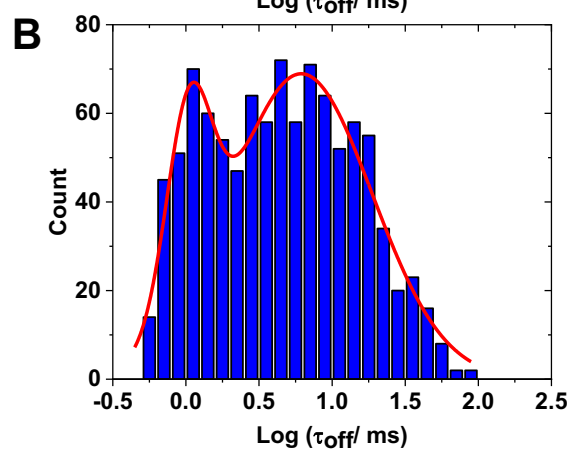
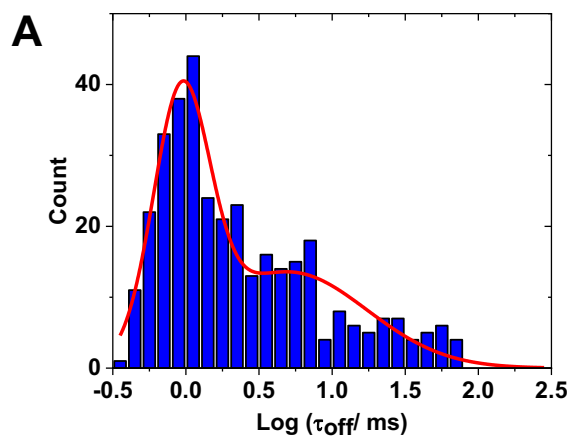


**Figure S11(ii)** Histogram of  $\tau_{on}$  at 75 mV for three different  $\alpha$ -CD concentration (A) 40  $\mu$ M,  $n=224$  (B) 200  $\mu$ M  $n = 1,032$  (C) 822  $\mu$ M,  $n = 250$ . Red solid curve in each histogram represent log-Weibull distribution fit. (D) Slope of  $1/\tau_{on}$  vs  $[\alpha\text{-CD}]$ , gives apparent association constant  $k_{on}$  between  $\alpha$ -CD and RNTP. Error bars are standard error in fitting the histogram.

**S12. Lifetime statistics of  $\alpha$ -CD interactions with an RNTP at different voltages. (A)**

**50mV, n = 405 (B) 75 mV, n = 998 (D) 100mV, n=349**



S13. All-atom MD simulation snapshots of  $\alpha$ -CD docked onto an RNTP.

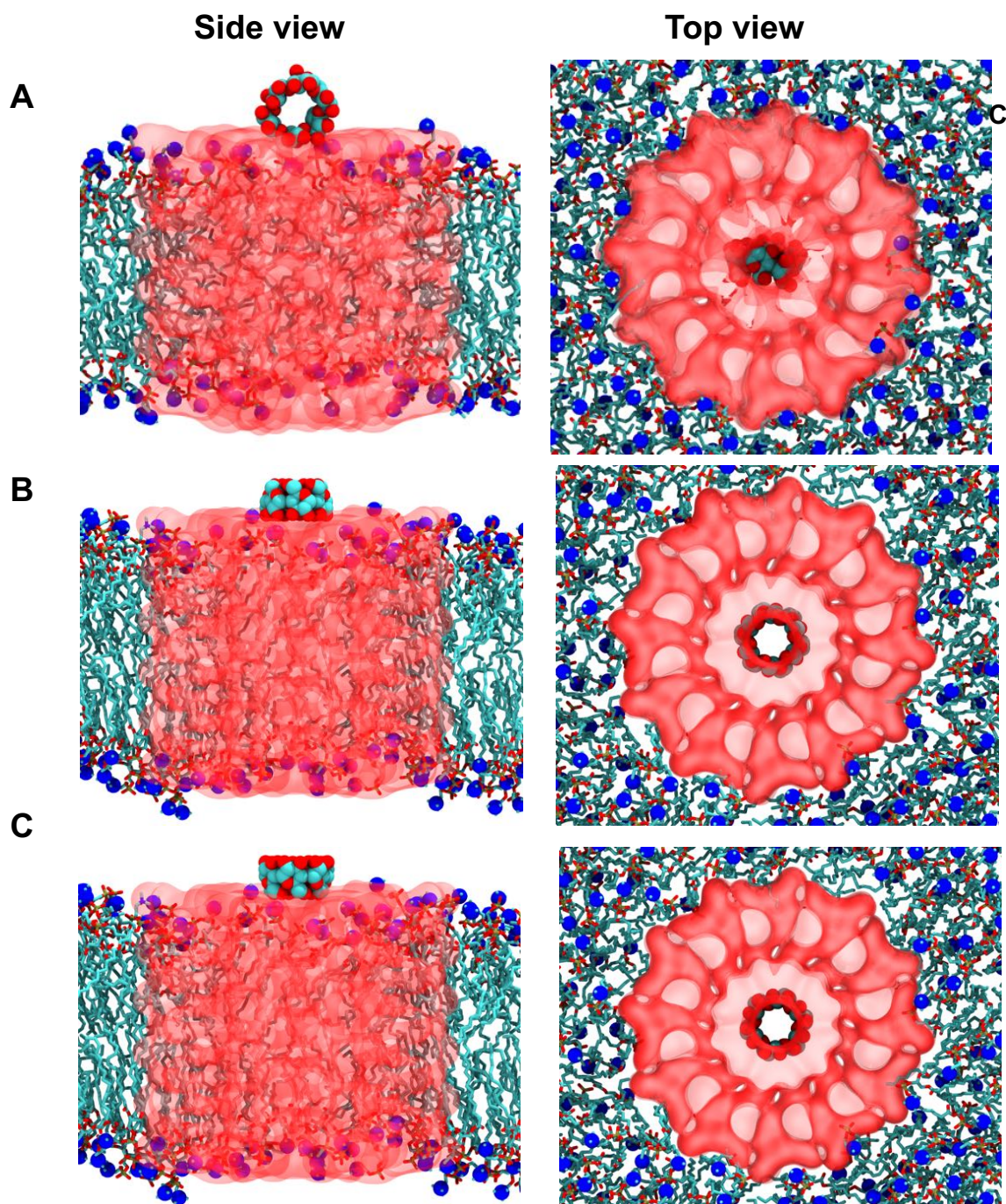


**Figure S13** All-atom models of  $\alpha$ -CD docked to an RNTP that is embedded in a POPC lipid bilayer membrane in three different binding conformations: (a) conformation i (b) conformation ii and (c) conformation iii. RNTP is shown as a red semi-transparent molecular surface whereas all oxygen and carbon atoms of  $\alpha$ -CD are shown as red and cyan spheres, respectively. The lipid molecules are shown in cyan color with the nitrogen atom of the headgroup highlighted by blue spheres. Water and ions are not shown.

#### S14. Residual ionic current of $\alpha$ -CD bound RNTP from MD simulations.

**Table S1.** The relative residual ionic current ( $I_b/I_o$ ), i.e. the ionic current when the  $\alpha$ -CD molecule is bound to RNTP divided by the open pore ionic current for three different conformation of  $\alpha$ -CD as shown in figure 3G or S13 using SEM . The obtained values of ionic conductance are in close agreement with the observed experimental results (Figure 3 A, B, C and D) of the current blockades produced by  $\alpha$ -CD.

Conformation of $\alpha$ -CD	Length of RNTP(nm)	Relative residual current
conf-1	6	0.18
conf-2	6	0.51
conf-3	6	0.51
conf-1	9	0.30
conf-2	9	0.75
conf-3	9	0.75

#### S15. All-atom MD simulation methodology.

All atom MD simulations were performed using the molecular dynamics program NAMD<sup>10</sup>. The initial atomistic structure of the three rings of a rosette nanotube porin (RNTP) were obtained from the first principle calculations. Repeating the geometrical transformation obtained from the optimized pdb structure, we built eleven planar rosettes stacked on top of each other to create an atomistic structure of RNTP 5 nm in length using VMD<sup>11</sup>, see Figures (2F-G, S10). The bonded and non-bonded interaction parameters for the repeating unit of a rosette were generated using the CHARMM general force fields<sup>12</sup> (CGenFF) webserver. We aligned the RNTP along the z axis and inserted into a  $11 \times 11$  nm<sup>2</sup> patch of pre-equilibrate 1-Palmitoyl 2-oleoyl-sn-glycero-3-phosphocholine (POPC) lipid bilayer membrane. The lipid patch was generated from the webserver of CHARMM-GUI membrane builder<sup>13</sup> and equilibrated for approximately 400 ns. We removed the lipid molecules overlapping with the RNTP. The system was then solvated using TIP3 water model<sup>14</sup> using the Solvate plugin of VMD<sup>11</sup>. Potassium (K<sup>+</sup>) and chloride (Cl<sup>-</sup>) ions were added using the Autoionize plugin of VMD to make electrically neutral solution of 0.6 M salt concentration. A similar system was built to contain 0.6 M solution of NaCl. Each final system was  $11 \times 11 \times 8.5$  nm<sup>3</sup> is volume and contained approximately 94,000 atoms.

The assembled systems were subjected to energy minimization using the conjugate gradient method that removed steric clashes among RNTP, lipid and solvent atoms. Following the energy minimization, the systems were subjected to equilibration at constant number of atoms (N), constant pressure (P=1 bar) and constant temperature (T=300 K), i.e., an NPT ensemble with harmonic restraints applied to all the non-hydrogen atoms of RNTP with respect to their initial coordinates; the restraint spring constant was 5 kcal/mol  $\text{\AA}^{-2}$ . The harmonic restraints were gradually reduced to 1 kcal/mol  $\text{\AA}^{-2}$ , 0.1 kcal/mol  $\text{\AA}^{-2}$  and 0 kcal/mol  $\text{\AA}^{-2}$  and subsequently the system was simulated without any restraints. The ratio of each system's dimensions was kept constant within the plane of the membrane (x-y plane); the system's dimension along z-axis was not constrained. The

simulations were performed using periodic boundary conditions and particle mesh Ewald (PME) method to calculate the long-range electrostatic over an X-A spaced grid. The Nose-Hoover Langevin piston<sup>15,16</sup> and Langevin thermostat were used to maintain the constant pressure and temperature in the system<sup>17</sup>. CHARMM36 force field parameters<sup>18</sup> described the bonded and non-bonded interactions of among lipid bilayer membranes<sup>19</sup>, RNTP, water and ions. A 8-10-12 Å cutoff scheme was used to calculate van der Waals and short range electrostatics forces. All simulations were performed using 2 femtosecond time steps for integrating the equation of motion. SETTLE algorithm<sup>20</sup> was applied to keep water molecules rigid whereas RATTLE algorithm<sup>21</sup> constrained all other covalent bonds involving hydrogen atoms. Several hundreds of nanosecond equilibrium MD simulations were performed for each system which give rise to transmembrane ion and water permeation. The coordinates of the system were saved at the simulation time interval of 9.6 ps. The analysis and post processing the simulation trajectories were performed using VMD<sup>11</sup> and CPPTRAJ<sup>22</sup>.

To probe the binding modes of alpha-cyclodextrin ( $\alpha$ -CD) to RNTP, we created three conformations of  $\alpha$ -CD docked on top of RNTP by varying the alignment of  $\alpha$ -CD with respect to the RNTP lumen, Figure 3(G) and S13. We employed the umbrella sampling technique<sup>23</sup> to calculate the potential of mean force<sup>24</sup> (PMF) between RNTP and  $\alpha$ -CD in different conformations. The distance of the center of mass of RNTP and center of mass of  $\alpha$ -CD along the bilayer normal (z-axis) was taken as the reaction coordinate for these PMF calculations. We created 10 sampling windows by varying the distance between  $\alpha$ -CD and RNTP along z-axis by 1 Å. In each window, the simulation was run for 10 ns; harmonic potential with a force constant of 4 kcal/mol/ Å<sup>2</sup> was applied to the  $\alpha$ -CD molecules to maintain its target z coordinate. Using weighted histogram analysis method<sup>25</sup> (WHAM), we obtained the unbiased PMF between RNTP and  $\alpha$ -CD.

Steric exclusion model<sup>26</sup> was used to compute the ionic current through the RNTP as well as the blockade current resulting from different placements of  $\alpha$ -CD molecule at the RNTP entrance.

## S16. SI References

1. Montal, M. and Mueller, P. Formation of Bimolecular Membranes from Lipid Monolayers and a Study of Their Electrical Properties. *Proc. Natl. Acad. Sci. USA* **1972**, *69*, 3561–3566.
2. Gutschmann, T.; Heimburg, T.; Keyser, U.; Mahendran, K. R.; Winterhalter, M. Protein reconstitution into freestanding planar lipid membranes for electrophysiological characterization. *Nature Protocols* **2015**, *10*, 188–198.
3. Burns, J. R.; Gopfrich, K.; Wood, J. W.; Thacker, V. V.; Stulz, E.; Keyser, U. F.; Howorka, S. Lipid-bilayer-spanning DNA nanopores with a bifunctional porphyrin Anchor. *Angew. Chem. Int. Ed.* **2013**, *52*, 12069 –12072.
4. Guo, Y.; Werner, M.; Seemann, R.; Baulin, V. A.; Fleury, J. Tension-Induced Translocation of an Ultrashort Carbon Nanotube through a Phospholipid Bilayer. *ACS Nano* **2018**, *12*, 12042–12049.

5. Ramadurai, S.; Holt, A.; Krasnikov, V.; Bogaart, G. V.; Killian, J. A.; Poolman, B. Lateral Diffusion of Membrane Proteins, *J. Am. Chem. Soc.* **2009**, 131 (35), 12650-12656.
6. Tunuguntla, R.; Henley, R. Y.; Yao, Y. C.; Pham, T. A.; Wanunu, M.; Noy, A. Enhanced water permeability and tunable ion selectivity in subnanometer carbon nanotube porins. *Science* **2017**, 357, 792–796.
7. David R. Lide, CRC Handbook of Chemistry and Physics (CRC Press, 2005)
8. Allgood, R. W.; Roy, D. J. L. E.; Gordon, A. R.; The Variation of the Transference Numbers of Potassium Chloride in Aqueous Solution with Temperature. *Journal of Chemical Physics* **1940**, 8, 418.
9. MacInnes, D. A.; Dole, M. The transference numbers of potassium chloride. New determinations of the Hittorf method and a comparison with results obtained by the moving boundary method. *J. Am. Chem. Soc.* **1931**, 53, 1357-1364.
10. Phillips, J. C.; Braun, R.; Wang, W.; Gumbart, J.; Tajkhorshid, E.; Villa, E.; Chipot, C.; Skeel, R. D.; Kale, L.; Schulten, K., Scalable molecular dynamics with NAMD. *Journal of Computational Chemistry* **2005**, 26 (16), 1781-1802.
11. Humphrey, W.; Dalke, A.; Schulten, K., VMD: Visual molecular dynamics. *J. Mol. Graph.* **1996**, 14 (1), 33-38.
12. Vanommeslaeghe, K.; Hatcher, E.; Acharya, C.; Kundu, S.; Zhong, S.; Shim, J.; Darian, E.; Guvench, O.; Lopes, P.; Vorobyov, I., CHARMM general force field: A force field for drug-like molecules compatible with the CHARMM all-atom additive biological force fields. *Journal of computational chemistry* **2010**, 31 (4), 671-690.
13. Lee, J.; Cheng, X.; Swails, J. M.; Yeom, M. S.; Eastman, P. K.; Lemkul, J. A.; Wei, S.; Buckner, J.; Jeong, J. C.; Qi, Y., CHARMM-GUI input generator for NAMD, GROMACS, AMBER, OpenMM, and CHARMM/OpenMM simulations using the CHARMM36 additive force field. *Journal of chemical theory and computation* **2015**, 12 (1), 405-413.
14. Jorgensen, W. L.; Chandrasekhar, J.; Madura, J. D.; Impey, R. W.; Klein, M. L., Comparison of simple potential function for simulating liquid water. *Journal of Chemical Physics* **1983**, 79 (2), 926-935.
15. Martyna, G. J.; Tobias, D. J.; Klein, M. L., Constant pressure molecular dynamics algorithms. *The Journal of Chemical Physics* **1994**, 101 (5), 4177-4189.
16. Feller, S. E.; Zhang, Y.; Pastor, R. W.; Brooks, B. R., Constant pressure molecular dynamics simulation: the Langevin piston method. *The Journal of chemical physics* **1995**, 103 (11), 4613-4621.
17. Brünger, A. T., *X-PLOR: version 3.1: a system for x-ray crystallography and NMR*. Yale University Press: 1992.
18. MacKerell Jr, A. D.; Bashford, D.; Bellott, M.; Dunbrack Jr, R. L.; Evanseck, J. D.; Field, M. J.; Fischer, S.; Gao, J.; Guo, H.; Ha, S., All-atom empirical potential for molecular modeling and dynamics studies of proteins. *The journal of physical chemistry B* **1998**, 102 (18), 3586-3616.
19. Klauda, J. B.; Venable, R. M.; Freites, J. A.; O'Connor, J. W.; Tobias, D. J.; Mondragon-Ramirez, C.; Vorobyov, I.; MacKerell Jr, A. D.; Pastor, R. W., Update of the CHARMM all-atom additive force field for lipids: validation on six lipid types. *The journal of physical chemistry B* **2010**, 114 (23), 7830-7843.

20. Miyamoto, S.; Kollman, P. A., Settle: An analytical version of the SHAKE and RATTLE algorithm for rigid water models. *Journal of computational chemistry* **1992**, *13* (8), 952-962.
21. Andersen, H. C., Rattle: A “velocity” version of the shake algorithm for molecular dynamics calculations. *Journal of Computational Physics* **1983**, *52* (1), 24-34.
22. Roe, D. R.; Cheatham, T. E., III, PTRAJ and CPPTRAJ: Software for Processing and Analysis of Molecular Dynamics Trajectory Data. *Journal of Chemical Theory and Computation* **2013**, *9* (7), 3084-3095.
23. Torrie, G. M.; Valleau, J. P., Nonphysical sampling distributions in Monte Carlo free-energy estimation: Umbrella sampling. *Journal of Computational Physics* **1977**, *23* (2), 187-199.
24. Roux, B., The calculation of the potential of mean force using computer simulations. *Computer Physics Communications* **1995**, *91* (1-3), 275-282.
25. Kumar, S.; Rosenberg, J. M.; Bouzida, D.; Swendsen, R. H.; Kollman, P. A., The weighted histogram analysis method for free-energy calculations on biomolecules. I. The method. *Journal of Computational Chemistry* **1992**, *13* (8), 1011-1021.
26. Wilson, J.; Sarthak, K.; Si, W., Gao, I.; Aksimentiev A., Rapid and accurate determination of nanopore ionic current using a steric exclusion model. *ACS Sensors*, **2019**, *4*(3):634–644.